Physics of the Earth and Planetary Interiors 320 (2021) 106787

Contents lists available at ScienceDirect

Physics of the Earth and Planetary Interiors

journal homepage: www.elsevier.com/locate/pepi

# Anatomy of seismicity clustering from parametric space-time analysis

Gianni Bressan, Carla Barnaba *, Antonella Peresan, Giuliana Rossi

*OGS - Istituto Nazionale di Oceanografia e di Geofisica Sperimentale, Trieste, Italy*

ARTICLE INFO

*Keywords:*
Seismicity
PCA analysis
Fractal dimension
Nearest neighbour distance
Shannon entropy
*B-value*
Damage pattern

ABSTRACT

A multi-parametric study of the space-time evolution of the seismicity from 2015 to the beginning of 2020 is performed within a well-focused area, located between the Alps and the Prealps, in the central part of the Friuli Venezia Giulia region (Northeastern Italy). The study area is characterized by a complex tectonic pattern resulting from the interference of differently oriented fault systems and involving mechanically heterogeneous rocks. From 2018 to 2019, the area experienced a significant increase and clustering of radiated seismic energy. The estimated damage pattern emphasizes the tectonic complexity. Notably, the most energetic events are located in correspondence with the sharp transitions from zones of low damage to zones of intermediate damage.

The evolution of seismicity is analyzed through the temporal variation of the Shannon entropy, *b-value*, fractal dimension, nearest neighbour distance, and changing orientation of the planes inferred from Principal Component Analysis (PCA). The PCA analysis is applied along a geological cross-section to infer the geometry and the time-evolution of the fracturing. It reveals best-fit planes mainly subvertical. Two distinct temporal phases are recognized, characterized by different orientation of planes and propagation of fracturing. The two phases correspond to the changes in the seismic activity, highlighted by the variations of the entropy, *b-value*, fractal dimension and nearest neighbour distance. The observed spatio-temporal evolution of seismicity is interpreted within the frame of damage evolution in a heterogeneous medium subjected to an applied remote stress.

## 1. Introduction

Time series, namely the temporal variations of different parameters quantifying seismicity with time, are among the most widely used tools to describe earthquake occurrence features within a region. Here, we propose a multi-parametric approach based on five differently analyses for investigating the space-time evolution of seismicity in areas characterized by complex tectonics, with the interference of different oriented faults and heterogeneous mechanical strength of the rocks.

Specifically, the variations of entropy, the *b-value* from the Gutenberg-Richter law (GR), the changes in fractal dimension, and the Nearest Neighbour distance ($\eta$), are used for assessing changes in the temporal patterns of seismicity. In contrast, the Principal Component Analysis (PCA), enables defining the geometry of the hypocentres distribution.

This study aims at characterizing the temporal changes of seismicity, from 2015 to the beginning of 2020, within a well-focused area located between the Carnic Alps and the Prealps and surrounding the Tolmezzo municipality (Northeastern Italy), through the application of the above-mentioned methods for the quantification of the seismicity temporal variations. In fact, after a long period of low seismic activity, lasting about 15 years, in 2018–2019, the Tolmezzo area experienced a significant increase of radiated seismic energy, spatially clustered, with four sequences induced by earthquakes with $M_D$ (coda-duration magnitude) ranging from 3.7 to 4.0 (http://www.crs.inogs.it/bollettino/RSFVG).

The study region and its surroundings are characterized by a relatively high seismic hazard and experienced several destructive earthquakes, the most recent one being the Mw = 6.41976 Friuli earthquake (Slejko et al., 1999). The most severe earthquakes that struck in the past the area around Tolmezzo (Rovida et al., 2016) occurred in: 1700 ($I_0$ = VIII-IX MCS on the Mercalli-Cancani-Sieberg scale, Mw = 5.7), 1788 ($I_0$ = IX, Mw = 5.2), 1928 ($I_0$ = IX, Mw = 6.0), 1959 ($I_0$ = VII-VIII, Mw = 5.2).

The instrumental seismic activity, recorded since 1977, is moderate, with a maximum $M_D$ 4.9 in 2002 (Bressan et al., 2018a). The seismicity is mainly located between 5 and 12 km depth (Bressan et al., 2016), and the predominant focal mechanism are of strike-slip and thrust type (Bressan et al., 2018a).

The geological structure of the study area is characterized by a

* Corresponding author.
*E-mail address:* cbarnaba@inogs.it (C. Barnaba).

https://doi.org/10.1016/j.pepi.2021.106787
Received 5 March 2021; Received in revised form 19 June 2021; Accepted 17 August 2021
Available online 1 September 2021

complex tectonic pattern as a result of the superposition of several tectonic phases that fragmented the crust into different tectonic domains (Venturini, 1991; Ponton, 2010). Marked mechanical heterogeneities characterize the upper crust (0–10 km depth), as evidenced by the 3D elastic moduli pattern obtained from the sequential tomographic integrated inversion of Bressan et al. (2012). The tomographic images revealed that the earthquake spatial distribution is strictly related to the sharp boundaries between rock mechanical heterogeneities. These findings suggest considering the occurrence of seismicity within a context of damage mechanics. In fact, the spatio-temporal fluctuations of the seismicity can be explained as the response of a mechanically heterogeneous medium to an applied tectonic stress field. In rock mechanics, the damage evolution and fracturing in heterogeneous brittle media result from the coupling between stress redistribution and variable heterogeneity of rocks on multiscale (Rong et al., 2006) with the appearance of damage clusters.

In order to investigate the time changes of earthquakes occurrence, we consider different parameters. We analyze the spatio-temporal evolution of the seismicity with the Shannon entropy, which quantifies the level of organization or disorder of an earthquake population (Telesca et al., 2004). We also include classical estimates of *b-value* as a function of time, the balance between small and large magnitude events, and the temporal variation of the fractal dimension to characterize the evolution of the spatial seismicity pattern. In addition, we analyze the "Nearest-Neighbour" distance by Baiesi and Paczuski (2004) as a measure of the correlation between earthquakes, which can also be used to characterize the clustering properties of seismicity (Zaliapin and Ben-Zion, 2013).

It is well known that the geometry of a fault is complex (Ben-Zion and Sammis, 2003), and the geometric variability provides different conditions of shear stress (Ben-Zion, 2001). Thomson et al. (2009) found in laboratory tests that the interaction between the main fault and secondary faults controls the stress concentration evolution. Therefore, we also investigated the evolution of the seismicity by inferring the orientation of the planes fitting the earthquake foci with the principal component analysis (PCA).

On the one hand, it is challenging to associate the recorded seismicity to a specific fault and to investigate the temporal evolution along faults in such a patched tectonic framework. On the other hand, Peresan and Gentili (2018) found that the region's instrumental seismicity is characterized by a dominant Poissonian component. This observation might affect the possible identification of an earthquake-fault causal connection. Still, it was demonstrated that the Poissonian features of the background seismicity are non-stationary, displaying significant variations over time (Benali et al., 2020). Therefore, we explore the spatio-temporal evolution of the seismicity through different methods and parameters to interpret it within the context of damage evolution.

## 2. Seismotectonic framework

The study area (Fig. 1) is located in the NE Italy, where the maximum interference pattern between the NW-SE oriented Dinaric overthrusts and the *E*-W oriented Alpine thrusts takes place. The counterclockwise rotation of the Adria microplate produced an active collision zone between the latter and Eurasia (Anderson and Jackson, 1987; Mantovani et al., 1996), and the imbrication and shortening of the Eastern Southalpine thrust belt (Castellarin and Cantelli, 2000). Three main tectonic phases can be recognized in time. The Mesoalpine (Dinaric) NE-SW compressional stage started in the Upper Cretaceous-Paleogene, the Neo-Alpine (Insubric) NNE-SSW compressional phase developed in the Chattian-Burdigalian, and the Valsuganese NNW-SSE compressions phase in the Serravalian-Tortonian age. The first stage generated folds and thrusts with southwestward vergence. The second phase displaced

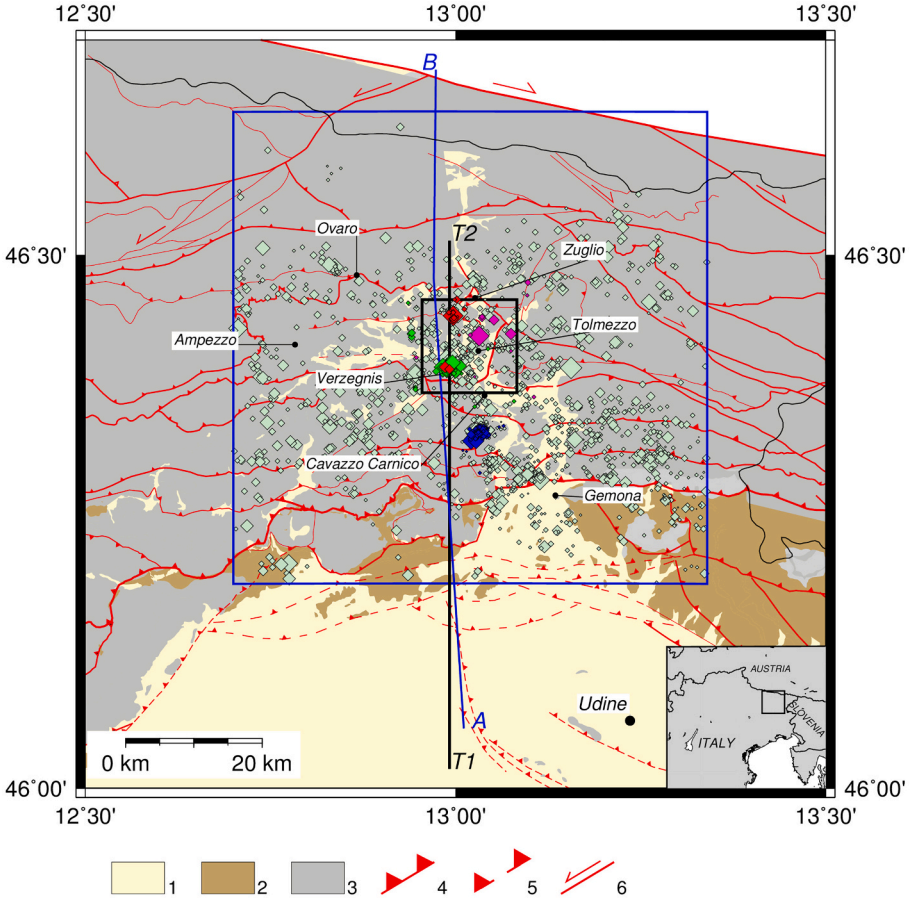


**Fig. 1.** Simplified tectonic and geological sketch of the study area, marked by a blue square. The small black square indicates the central cell of the grid including the clustering of most radiated seismic energy, where Shannon entropy was computed. Symbols: 1) Quaternary cover, 2) Flysch (Upper Maastrichtian-Middle Eocene) and molasse sequence (Miocene); 3) Ordovician-Maastrichtian bedrock; 4) Thrusts; 5) Buried or blind thrusts; 6) High-angle strike-slip faults. Light green diamonds: background seismicity from 2015 to March 2020. The values of magnitude are given in coda-duration magnitude $M_D$. Fuchsia diamonds: earthquakes pertaining to the January 19, 2018, $M_D$ 3.8 (E1) sequence. Blue diamonds: earthquakes of the August 11, 2018, $M_D$ 3.9 (E2) sequence. Green diamonds: earthquakes of the June 14, 2019, $M_D$ 4.0 (E3) sequence. Red diamonds: earthquakes pertaining to the September 22, 2019, $M_D$ 3.8 (E4) sequence. A-B: trace of the geological cross-section. It corresponds to the geological cross-section S3 of Bressan et al. (2016). T1 – T2: trace of the tomographic cross-section where the pattern of damage has been elaborated. It corresponds to the N-S grid node X = −7 of Bressan et al. (2016). (For interpretation of the references to colour in this figure legend, the reader is referred to the web version of this article.)

the former Dinaric thrusts and partially reactivated and counterclockwise rotated their fronts. The last stage generated the WSW-ENE-oriented thrusts and backthrusts (Ponton, 2010).

In particular, the study area (including the Tolmezzo area), located in the northern part of the Friuli Venezia Giulia region of Italy, is characterized by a complex geological setting (Carulli, 2000). Here, the E-W oriented Alpine thrusts, and backthrusts superimpose the NW-SE oriented Dinaric thrusts; the maximum interference between the two systems occurs from the surface to about 10–12 km depth (Ponton, 2015; Bressan et al., 2016). The extended Plio-quaternary fluvioglacial deposits mask the outcropping rocks. The Permo-Triassic thick and stiff carbonate platform rocks and a small outcrop of Carnian shallow-water deposits (thinly laminated dolomites, marly sandstones, and gypsum) are present (Carulli, 2006). Interferences and reciprocal influences are difficult to interpret, so different structural models have been proposed (Carulli, 2000; Ponton, 2010; Poli and Zanferrari, 2018). Leaving aside the interpretative speculations, normal faults with a NNE-SSW trend, inverse N-dipping and S-dipping faults with an E-W trend have been recognized. There are also some strike-slip faults, with a NE-SW trend, which segment the previous structures.

The geological cross-section S3 (Fig. 2) points out the geometrical relation between the tectonic phases (Ponton, 2010). The section is N-S oriented, orthogonal to the Neoalpine faults, and oblique to the Dinaric faults. The Neoalpine structures, widely south-verging, obliquely cut the Dinaric structures, NE dipping, partially reactivating their fronts.

The extended quaternary coverage plays an essential role in evaluating the magnitude of the past events because of the amplification of the ground shaking by local site conditions (Barnaba et al., 2010).

The inversion of the focal mechanisms enlights a transpressive stress regime for the stress field of the Tolmezzo area. The comparison between the stress and strain tensors evidenced planes of mechanical weakness, variously oriented, often not favourably with respect to the principal axes of stress, suggesting a heterogeneous crustal strength (Bressan et al., 2018a).

## 3. Data analysis

The map in Fig. 1 shows the analyzed seismicity with the marked sequences, the trace of the geological cross-section, and the vertical cross-section trace, where the damage pattern has been elaborated. The seismicity is spatially distributed, with localized clusters not only pertaining to aftershock sequences. The choice of the extent of the area has been driven by the calculation of the Shannon entropy, as explained in the chapter regarding the multi-parametric temporal analysis of seismicity.

The seismicity data set consists of 1493 earthquakes that occurred from 2015 to March 2020 with coda-duration magnitude $M_D$, computed according to Rebez and Renner (1991), ranging from 0.4 to 4.1.

The earthquakes were relocated based on the 3D P-wave and S-wave velocity model of Bressan et al. (2012). The means of the standard errors relative to the hypocentral coordinates are: 0.07 km for x coordinates, 0.07 km for y coordinates, and 0.23 km for depth; the distribution of standard errors is shown in Fig. 3.

The distribution of the number of events as a function of magnitude is shown in Fig. 4. Different techniques are available to assess the threshold of magnitude completeness $M_{DC}$ (e.g., Mignan and Woessner, 2012 and references therein), most of which are based on the assumption of log-linearity of the frequency-magnitude distribution of earthquakes, according to the Gutenberg-Richter law (GR; Gutenberg and Richter, 1944). Based on visual inspection of the cumulative and discrete distributions for events in 2015–2019 (Fig. 4a), the completeness threshold can be estimated around $M_{DC} = 0.9$–$1.0$; below this threshold, in fact, the number of events does no longer increase. To get a deeper insight into the data, for each year, we examined the distribution of the events' number versus magnitude, considering both the cumulative and the discrete representations (Fig. 4b and c). Except for 2015, for which the discrete distribution of the events shows an evident deviation from the log-linearity, with a relatively high number of events for $M_{DC} =$ 1.8–2.0, the event distribution follows the GR law (Fig. 4c). For most of the remaining years, a bent in the frequency-magnitude distribution can be observed for magnitudes below $M_{DC} = 1.0$. Accordingly, a relatively homogeneous completeness threshold can be confidently fixed, over the entire period 2015–2019, as $M_{DC} = 1.0$. This threshold, inferred from visual data inspection, is in good agreement with $M_{DC} = 0.9$ formal estimate based on the Shi and Bolt (1982) method, which, however, does not account for the evidenced year-by-year variability. The number of earthquakes selected for $M_{DC} \geq 1.0$ is 738, out of a total number of events (1493) occurred within the study area. Based on the complete set

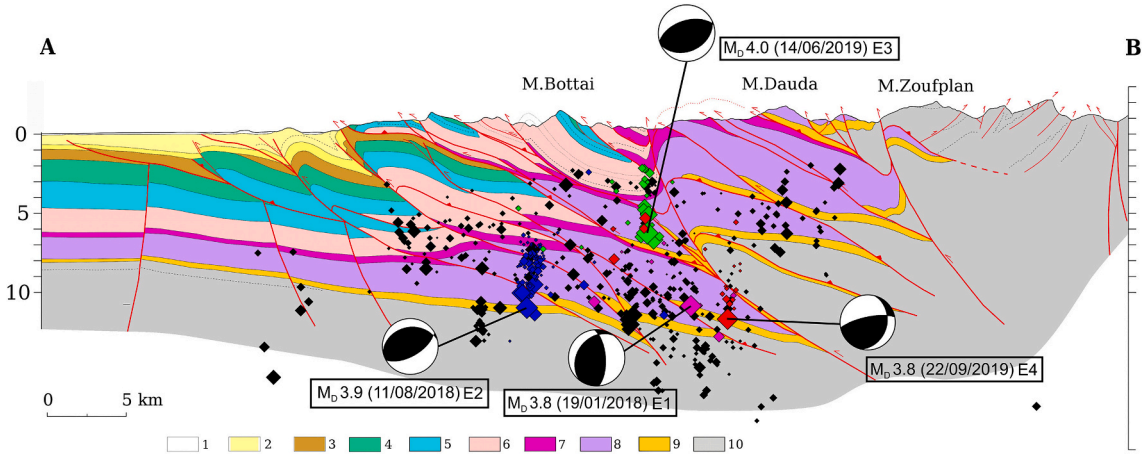


**Fig. 2.** Geological cross-section A-B. 1: Quaternary deposits; 2: molasse deposits; 3: flysch deposits and carbonatic levels (Upper Cretaceous- Eocene); 4: Cretaceous limestones; 5: Jurassic limestones; 6: Upper Triassic dolomitic rocks and massive limestones; 7: Upper Triassic evaporitic, terrigenous and carbonatic rocks; 8: Lower Triassic prevailing limestones; 9: Upper Permian carbonatic, marly, and evaporitic rocks; 10: Paleozoic terrigenous, carbonatic and locally volcanic deposits; red lines: faults (modified from Ponton, 2010). Black diamonds: background earthquakes. Aftershocks pertaining to January 19, 2018, $M_D$ 3.8 mainshock (E1): fuchsia diamonds. Aftershocks of the August 11, 2018, $M_D$ 3.9 mainshock (E2): blue diamonds. Aftershocks induced by the June 14, 2019, $M_D$ 4.0 mainshock (E3): green diamonds. Aftershocks of the September 22, 2019, $M_D$ 3.8 mainshock (E4): red diamonds. The inset shows the coda duration-magnitude $M_D$ of the mainshocks and the time occurrence. The mainshocks focal mechanisms are shown, displayed as lower hemisphere equal-area projection, not projected in the section plane. The seismicity within ±5 km from the section is plotted. (For interpretation of the references to colour in this figure legend, the reader is referred to the web version of this article.)

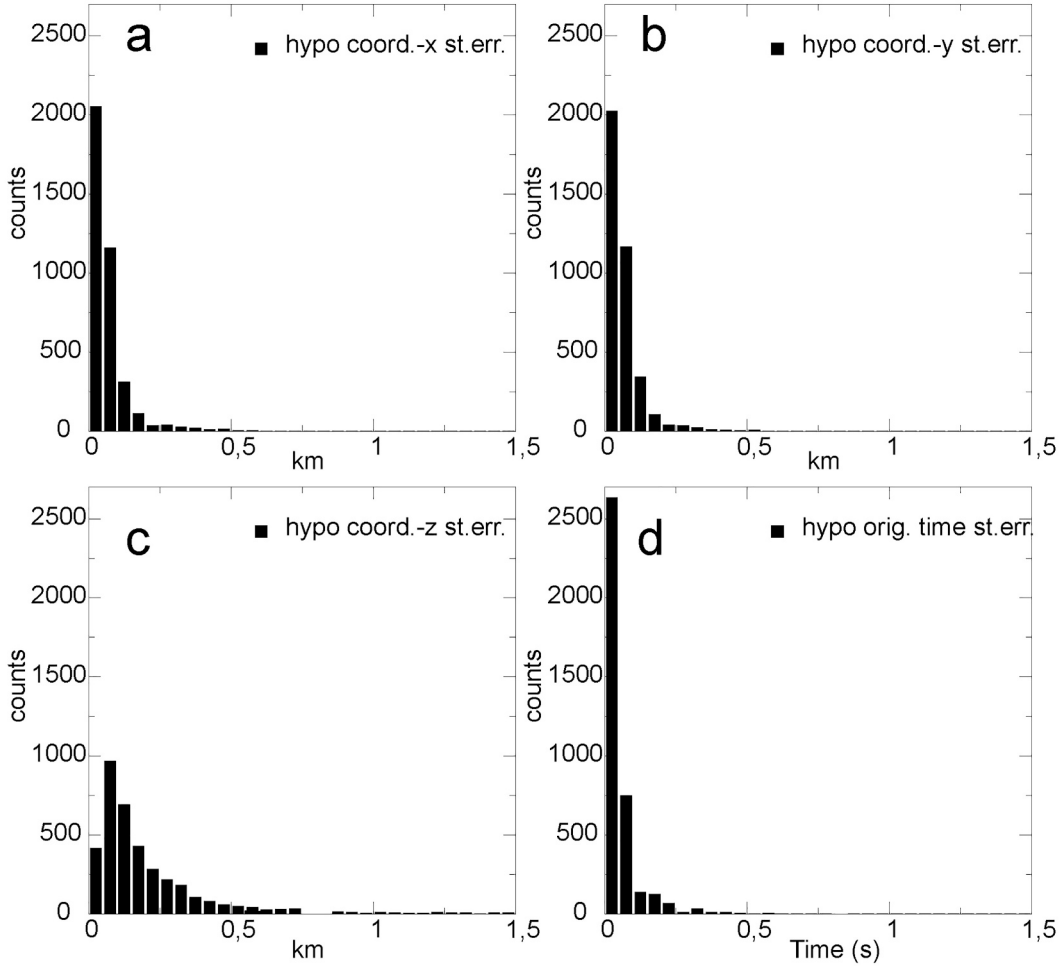


**Fig. 3.** Histograms showing the hypocentral errors versus the number of the relocated earthquakes. a: standard errors relative to X coordinates; b: standard errors relative to Y coordinates; c: standard errors relative to the depth; d: standard errors relative to the origin time.

of events with $M_D \geq M_{DC} = 1.0$, the coefficients of the linear relation $LogN(M) = a\text{-}bM$ are as follows: $b = 0.72 \pm 0.02$ with $a = 3.56$ according to maximum-likelihood estimates, and $b = 0.79 \pm 0.01$ with $a = 3.67$ by weighted least-squares technique (Wiemer, 2001); the corresponding fit lines are shown in Fig. 4a. Accordingly, the long-term estimate of the *b-value* for the entire time interval 2015–2019 can be grossly evaluated to fall within the range [0.7–0.8]; such values are relatively low if compared with the *b-value* = 0.9, estimated over a larger space-time scale, namely for the entire Friuli Venezia Giulia region in 1995–2018 (Peresan and Gentili, 2018).

We consider the catalogue with $M_D \geq M_{DC} = 1.0$ to investigate the temporal variability of: Principal Component (PCA), *b-value*, fractal dimension, nearest-neighbour distance $\eta$, and Shannon entropy.

In the analyzed time interval, four events with magnitude greater than 3.7 occurred: the 2018 January 19 with $M_D = 3.8$ (E1 in the following); the 2018 August 11 with $M_D = 3.9$ (E2 in the following); the 2019 June 14 with $M_D = 4.0$ (E3 in the following); 2019 September 22 with $M_D = 3.8$ (E4 in the following).

The seismicity within a band extending laterally ±5 Km, is plotted on the geological cross-section (Fig. 2). The PCA analysis includes the seismicity along the geological cross-section. The purpose is to retrieve the time evolution of the geometry of the planes fitting the earthquake foci and to ensure a comparison with the known fault geometries.

## 4. Damage model

The inelastic behaviour of crustal rocks under loading stress can be referred to the concept of damage (Kachanov, 1986). The damage can be expressed with a variable that describes the irreversible deformation as the progressive degradation of the physical and mechanical properties with the ongoing strain (Krajcinovic, 1996). Following this approach, the seismicity pattern appears to be related to the spatial variation of the crust's mechanical properties that can be represented by a damage variable.

Fig. 5 shows the pattern of damage along the cross-section T1-T2 (Fig. 1) and the seismicity plotted within a band extending laterally ±5 Km. The pattern of damage has been elaborated in Bressan et al. (2016), by calculating the values of damage at the grid nodes of the 3D seismo-gravity integrated inversion performed by Bressan et al. (2012). The procedure is summarized as follows.

The damage D was calculated using the scalar relation between the effective shear modulus $G_{eff}$ of a reference material and the shear modulus of damaged materials $G_D$ from:

$$G_D = (1 - D)\, G_{eff} \quad (1)$$

The effective shear modulus of the reference material $G_{eff}$ was obtained from laboratory measurements on the most representative lithologies of the Friuli upper crust (Faccenda et al., 2007). We used the values calculated from measurements of the seismic intrinsic properties at 400 MPa confining pressure because it is well above the corresponding pore and microfracturing closing level (150–200 MPa). The shear modulus of the damaged rocks $G_D$ was obtained from the 3-D sequential integrated inversion of tomographic images and gravity data (Bressan et al., 2012). The lithotypes were assigned at each grid

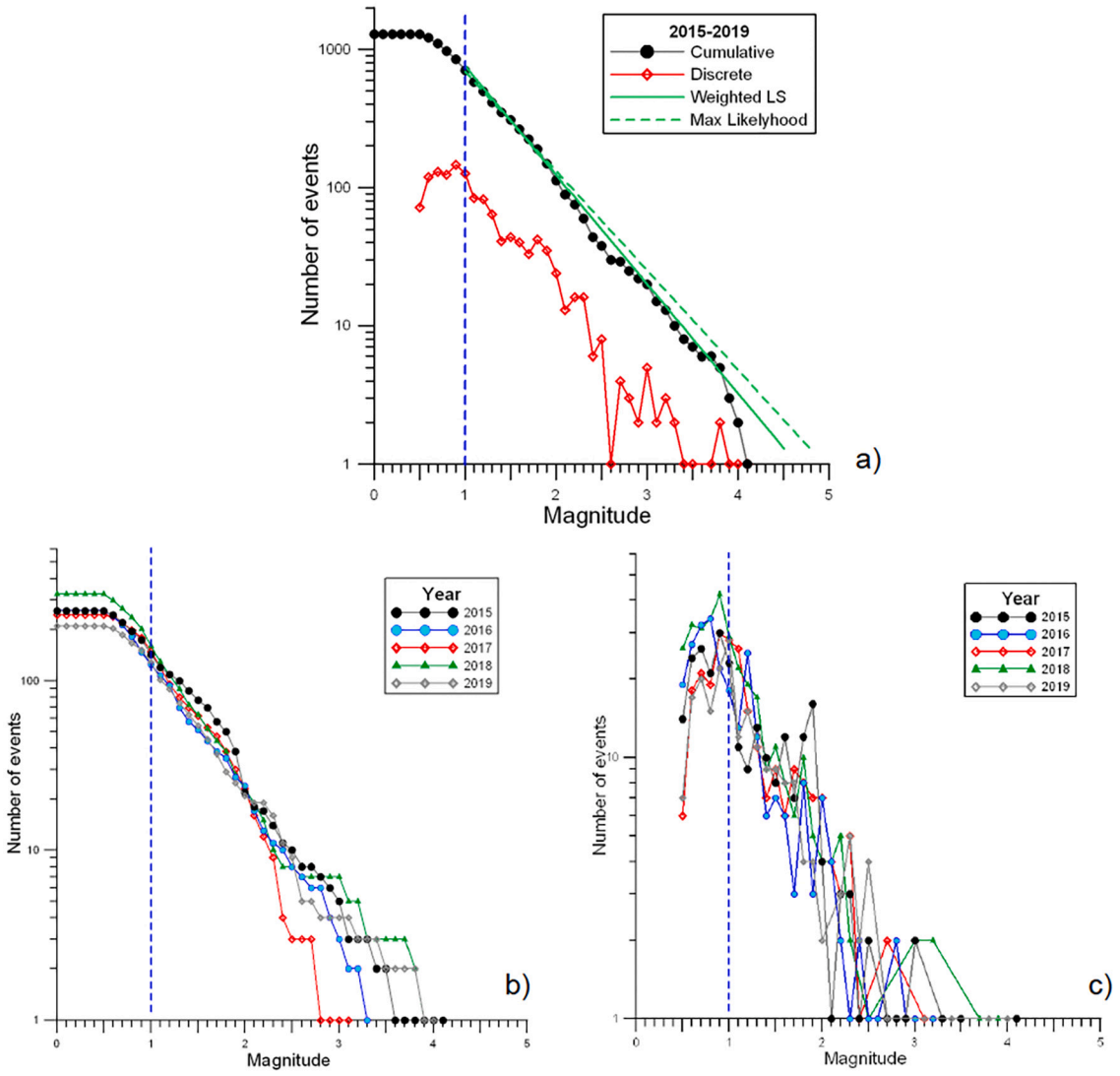


**Fig. 4.** Completeness analysis for OGS earthquake data in the study area: (a) frequency-magnitude distribution and linear fits (green lines) for events with $M_D \geq M_{DC} = 1.0$, computed by ZMAP6.0 software (Wiemer, 2001); b) Yearly cumulative distributions of events vs magnitude; c) Yearly discrete distributions of events vs magnitude. The completeness threshold Mc = 1.0 is marked in each plot (vertical dashed blue line). (For interpretation of the references to colour in this figure legend, the reader is referred to the web version of this article.)

node of the 3-D seismo-gravity integrated model according to the geometries and thickness of the sedimentary units, outlined through the geological cross-sections of Ponton (2010, 2015).

In short, the shear modulus of the uncracked rocks was obtained from laboratory measurements at 400 MPa confining pressure, while the seismo-gravity inversion provided the shear modulus of the cracked rocks.

The damage pattern (Fig. 5) is characterized by high heterogeneity and spots with sharp variations, attributed to the alternation of high-stiffness rocks and lower-stiffness rocks, caused by overthrusting (Bressan et al., 2016), as shown in Fig. 2. High-stiffness rocks pertain to the upper Triassic dolomitic rocks with in-situ shear modulus values in the range 2.80–3.80 $\times 10^{10}$ $Nm^{-2}$. Low-stiffness rocks generally consist of Jurassic limestones with in-situ shear modulus in the range 2.30–3.0 $\times 10^{10}$ $Nm^{-2}$. Generally, low damage areas correspond to high shear modulus and vice versa (Bressan et al., 2016).

The seismicity, particularly the events with the highest energy release, appears mostly located in correspondence of the sharp transition from zones of low damage to zones of intermediate damage.

## 5. Multi-parametric temporal analysis of seismicity

### 5.1. Temporal variation of the Shannon Entropy

The space-time organization and evolution of an earthquake population can be described by the Shannon's information entropy (Shannon, 1948), that measures the level of disorder of a system, providing the deviation from a uniform distribution (Telesca et al., 2004). Bressan et al. (2017) investigated with the normalized Shannon entropy the spatio-temporal evolution of eight seismicity populations in north-eastern Italy and western Slovenia, preceding and following moderate shocks with $M_D$ in the range [4.1–5.6].

Their spatio-temporal pattern was similar. The earthquakes are quite widespread before the mainshock. The seismicity is vanishing all around the aftershock cluster during the sequence, and it is again spread over the whole area after the sequence.

This spatio-temporal variability appears not significant at a distance larger than 30 km from the mainshock location (Peresan and Gentili, 2018) and allowed to design the extent of the area in which to analyze the seismicity as a thermodynamic system. In the present study, we

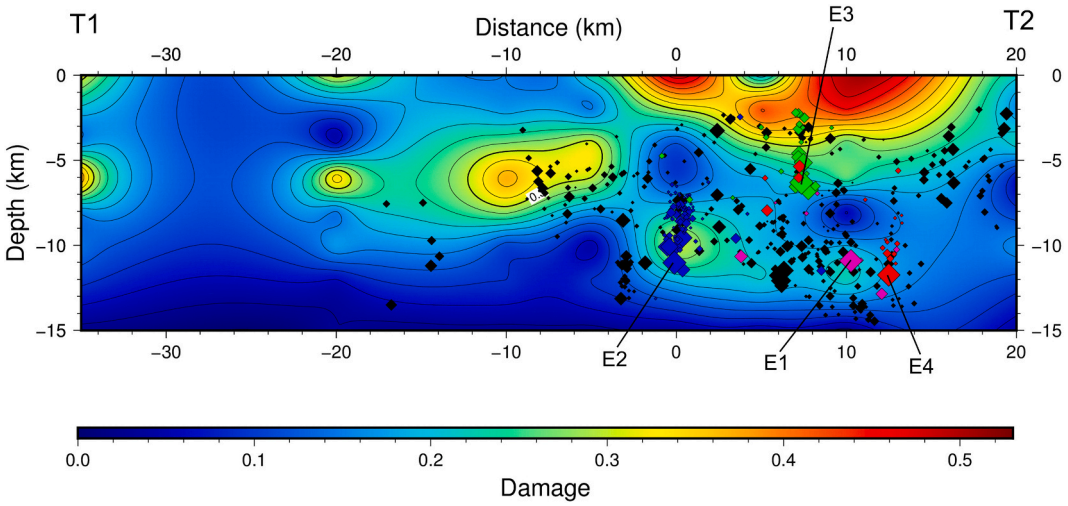


**Fig. 5.** Damage pattern along the cross-section T1-T2. It corresponds to the original section X = -7, N-S oriented of the 3D seismo-gravity integrated inversion of Bressan et al. (2012). Black diamonds: background seismicity. Fuchsia diamonds: earthquakes pertaining to January 19, 2018, $M_D$ 3.8 (E1) sequence. Blue diamonds: earthquakes of the August 11, 2018, $M_D$ 3.9 (E2) sequence. Green diamonds: earthquakes of the June 14, 2019, $M_D$ 4.0 (E3) sequence. Red diamonds: earthquakes pertaining to the September 22, 2019, $M_D$ 3.8 (E4) sequence. The seismicity within ±5 km from the section is plotted. (For interpretation of the references to colour in this figure legend, the reader is referred to the web version of this article.)

maintain the same size of the area for the multiparametric analysis of the temporal variations of other parameters quantifying the seismicity, namely the b-value, the fractal dimension, the Nearest Neighbour distance.

We followed Bressan et al. (2017)'s approach to calculate the Shannon entropy *h* from the variation of the radiated seismic energy within the study area. For this purpose, the area was subdivided into a 3-D regular grid of 50 cells, each with size 10x10x10 km, with the central grid including the clustering of most radiated seismic energy, close to Tolmezzo. The Shannon entropy was normalized to obtain an index *h* in the range [0;1] that allows comparing time intervals with different radiated seismic energy. The lowest level of predictability of a system occurs when the normalized Shannon entropy is $h = 1$, since all the states are equiprobable. The normalized Shannon entropy decreases with increasing order, and the system has the highest predictability when $h = 0$. To follow the system time evolution, we performed the analysis by sliding a temporal window of size $N = 30$ events, with the shift of one event, as done in previous analyses (Bressan et al., 2017) and confirmed on tests for the fractal dimension analysis, described in the following (Fig. 8).

The Shannon entropy (Fig. 6) oscillates around the value 0.7 with

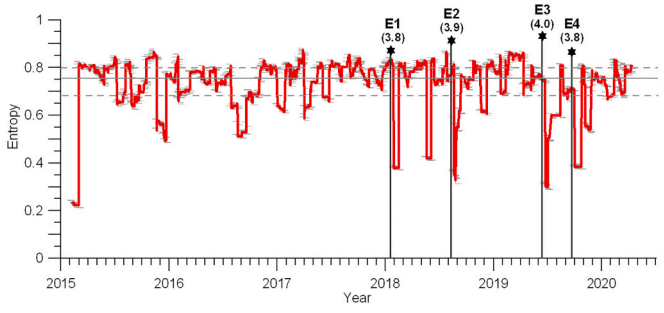


**Fig. 6.** Time variation of the Shannon entropy in January 2015 – March 2020, $M_C = 1$. Earthquakes with magnitude $M_D > 3.7$ are marked by stars with the corresponding magnitudes. The horizontal grey lines show the median (continuous line) and the first and third quartiles (dashed lines). The occurrence of earthquakes with magnitude $M_D > 3.7$ is marked by stars, with the corresponding labels E1, E2, E3, E4, and the coda duration magnitude in parentheses.

small temporary local decreases between July 2015 and July 2017, caused by clusters of higher seismic radiated energy. From January 2018 to January 2020, we observe marked decreases corresponding to the mainshocks (E1, E2, E3, E4) and related aftershocks that occurred close to the town of Tolmezzo, with the entropy *h* dropping to 0.3 and recovering the value 0.7 after September 2019. The temporary decrease in May 2018 corresponds to an $M_D$ 3.6 earthquake, located about 25 km at SE of Tolmezzo town.

### 5.2. *Changes of b-value with time*

In order to analyze the changes of *b-value* as a function of time, the parameter *b* was computed within sliding time windows of variable duration, containing a fixed number N = 30 of earthquakes and shifted by one earthquake. A such number of events allowed obtaining sufficiently stable temporal patterns avoiding undue smoothing and loss of details related to larger values of N (tests performed with $N = 50$, not presented here, provided well consistent, though less detailed results). The *b-value* was estimated by the maximum likelihood technique, based on the mean magnitude of all the earthquakes with magnitude $M \geq Mmin = Mc = 1.0$ (Aki, 1965).

The temporal variations of the *b-value* are shown in Fig. 7a. An increasing trend, from b = 0.7–0.8 to about b = 1.0, can be observed from 2015 to around mid-2017. During the second half of 2017, the *b-value* decreases progressively, reaching a relative minimum just before the E1 $M_D$ = 3.8 event on January 19, 2018; afterwards, it displays significant fluctuations around relatively low values. Starting with the E2 $M_D$ = 3.9 earthquake on August 11, 2018, the *b-value* increases considerably, reaching its maximum value (approximately b = 1.2–1.4) around March 2019. Subsequently, in March–June 2019, a rapid decrease of the *b-value* is observed, which brings it back to the lowest values obtained since 2015 (i.e., b = 0.6–0.8); on June 14, 2019 an $M_D$ = 4.0 earthquake is reported (E3), followed by a $M_D$ = 3.8 event on September 22 (E4). The *b-value* remains low (i.e., below the median) until the beginning of 2020, when a positive trend is detected. Generally, a negative trend of the *b-value* can be observed before the most energetic events (Fig. 7a). The stability of the identified *b-value* temporal changes has been verified using different techniques (e.g., Shi and Bolt, 1982), as well as a different grouping of events N and time-shift; the resulting pattern (not shown here) turns out well consistent with the variations illustrated in Fig. 7a.

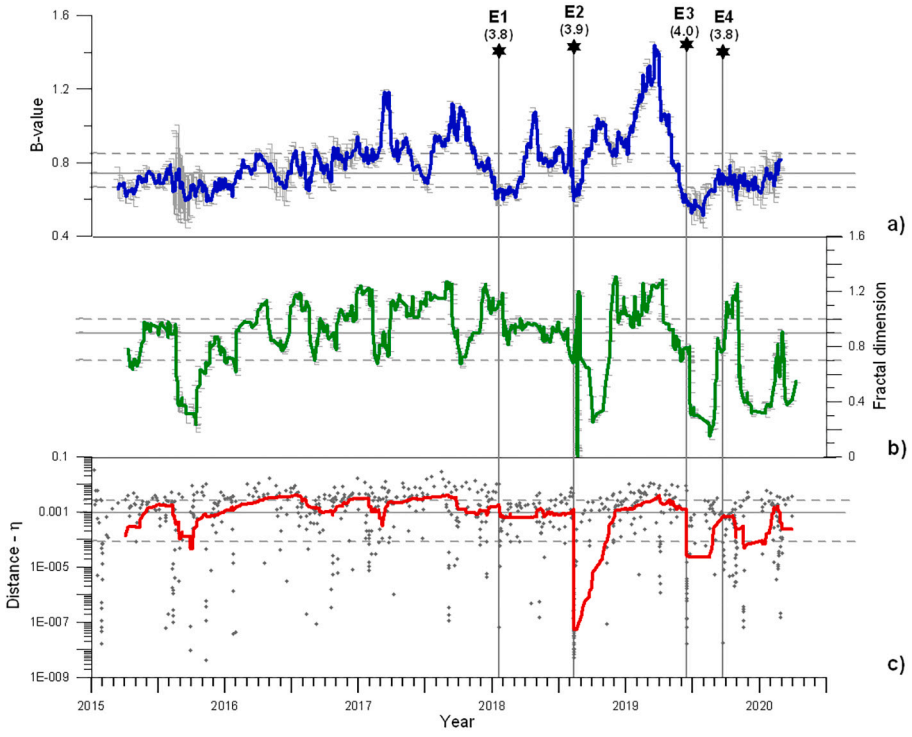


**Fig. 7.** Temporal variation of the *b-value* (a), fractal dimension (b), Nearest-neighbour distances $\eta_{ij}$ (c), estimated for earthquakes with $M_D > Mc = 1.0$ within the study area. The *b-values* are computed by the maximum likelihood technique with fixed $M_{min} = 1.0$, as implemented by ZMAP6.0 software (Wiemer, 2001). The running averages of each variable are computed for groups of $N = 30$ events, with shift = 1 event. The median (continuous grey line) and the first and third quartiles (grey dashed lines) are shown for *b-value* and fractal-dimension time series. The distances $\eta$, between each earthquake and its nearest-neighbour event (grey dots) are shown along with their running average (red line). Stars mark the occurrence of earthquakes with a magnitude $M_D > 3.7$, with the corresponding labels E1, E2, E3, E4, and $M_D$ magnitude in parentheses. (For interpretation of the references to colour in this figure legend, the reader is referred to the web version of this article.)

### 5.3. Temporal changes in the fractal dimension of hypocentres

The fractal analysis of a seismic catalogue enables describing with a single number distribution characteristics, e.g., the clustering. The non-integer values of the fractal dimension $D_c$ can be interpreted in relation to the Euclidean dimensions describing a point (0), a line (1), a plane (2), and a sphere (3). Values close to zero indicate a high level of clustering around a point, whereas increasing values indicate the tendency to a linear or planar distribution or even to fill an entire volume (Mandelbrot, 1977).

We chose the fixed-size Correlation Integral method (Mandelbrot, 1977; Grassberger, 1983) to calculate the fractal dimension of the spatial distribution of the seismic events, since it is less sensitive to data number and shape of the point spatial distribution than other methods, and, hence, suitable to analyze small datasets or limited regions (Hirata et al., 1987; Havstad and Ehlers, 1989; Rossi, 1990; Theiler, 1990; Molchan and Kronrod, 2005; Kagan, 2007).

According to the Correlation Integral method, the fractal dimension $D_c$ is:

$$D_f = \lim_{L \to 0} \frac{logC(L)}{logL} \tag{2}$$

while

$$C(L) = \frac{n}{N} \tag{3}$$

where $n$ is the number of couples of hypocentres separated by a distance less than $L$, progressively reduced, and $N$ is the total number of events. Hence, $D_c$ is the slope of the curve of $C(L)$ versus $L$ in a bi-logarithmic diagram. Operating on a limited region, we avoid the large distances at which the algorithm could saturate (Theiler, 1986; Eneva, 1996; Bressan et al., 2016).

As Bressan et al. (2017), we tested different sliding-window widths to perform the analysis, evaluating the order of magnitude of the distances between couples of events. We chose a window width implying a distance range of more than two orders of magnitude, i.e., of category A, according to Bressan et al. (2016). Fig. 8 shows that for windows larger than 10 events, the curve (distance range vs. window width) tends to flatten. On this basis, we chose a window of $N = 30$ events, also for homogeneity with previous studies (Rossi, 1990; Rossi, 1994; Bressan et al., 2017). The time variation of the fractal dimension is shown in Fig. 7b.

The spatial fractal dimension decreases sharply since August 2015, with values as low as 0.25, and then recovers values close to 1 in December 2015. Since the beginning of 2016 and until the end of 2017, the fractal dimension slightly oscillates around 1. Then, we observe remarkable oscillations until March 2020, with values decreasing to 0.25 and increasing again to 1.2. A first marked decrease is, in fact, observed at the end of 2017, followed by a steep rise just before the E1

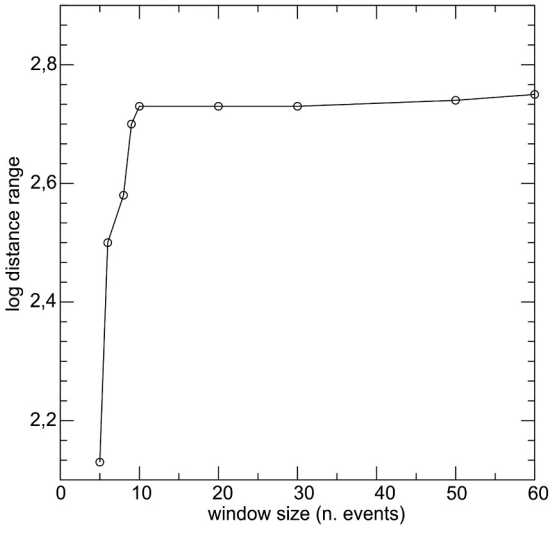


**Fig. 8.** Distance range (logarithm) vs the window width (number of events), considering the events larger or equal to the completeness magnitude threshold $M_C = 1$.

earthquake (January 2018). The values keep lower than 0.8 until the E2 earthquake (August 2018), after which we observe a sharp decrease to values around 0.25. The rise to values greater than 1 occurs since November 2018. A new decrease starts in April 2019, before the E3 earthquake (June 2019), and continues, with values around 0.1, until the end of July 2019. The fractal dimension starts to increase before the E4 (September 2019). After the E4 event, the fractal dimension decreases again, reaching values smaller than 1 in October 2019, still observed in 2020.

### 5.4. Temporal variations of Nearest Neighbour distance between earthquakes

We examined the temporal variability of earthquake clustering properties within the study area, based on a generalized definition of distances between pairs of events in the time–space–magnitude domain, namely, the Nearest-Neighbours distance $\eta$ introduced by Baiesi and Paczuski (2004). Following Zaliapin et al. (2008), given an earthquake catalogue, where each event $i$ is characterized by its occurrence time $t_i$, latitude, longitude, depth, and magnitude, the generalized distance $\eta_{ij}$ between a given earthquake $j$ and an earlier earthquake $i$ is defined as:

$$\eta_{ij} = \left\{ t_{ij} r_{ij}^{\overline{d_f}} 10^{-\overline{b} m_i}, \infty, \right\} \begin{matrix} t_{ij} 0 \\ t_{ij} 0 \end{matrix} \quad (4)$$

where: $t_{ij} = t_j - t_i$ is the inter-occurrence time between earthquakes $i$ and $j$ $(i < j)$; $r_{ij}$ is the spatial distance between epicentres; $\overline{d_f}$ is the fractal dimension of epicentres; $b$ is the *b-value* parameter (slope) of the Gutenberg-Richter law (Gutenberg and Richter, 1944). The event $i^*$ is the nearest neighbour of event $j$, if it corresponds to the minimal distance between $j$ and all earlier events $i$. The nearest neighbour $i^*$ is referred to as the *parent* of the event $j$; each event has a single parent and can be the parent of multiple events, called its *offsprings*.

According to Baiesi and Paczuski (2004), $\eta_{ij}$ provides a metric to quantify the correlation between any two earthquakes. In fact, based on eq. (4) which defines $\eta_{ij}$, they argue that out of all the earthquakes preceding $j$ "the most unlikely to occur is earthquake $i^*$, such that $\eta_{ij}$ is minimized when $i = i^*$. However, $i^*$ earthquake actually occurred relatively to $j$, even though it was the least likely to have done so. Therefore, $i^*$ must be the event to which earthquake $j$ is most correlated. In general, if $\eta_{ij} << 1$, then the correlation between $j$ and $i$ is very strong, and vice versa. By this argument, the correlation $c_{ij}$ between any two earthquakes $i$ and $j$ is inversely proportional to $\eta_{ij}$, or: $c_{ij} = 1/\eta_{ij}$ ".

This property can also be used for earthquake clusters identification; in fact, by setting a threshold distance $\eta_o$, events $i$ and $j$ are considered weakly linked if $\eta_{ij} > \eta_o$ (i.e., if their distance is high, correlation is low); vice versa, if distance $\eta_{ij}$ is low, the events are strongly linked. Thus, the removal of weak links leads to identifying clusters of events (Zaliapin et al., 2008; Zaliapin and Ben-Zion, 2013).

We analyzed the temporal variations of the nearest neighbour distances by considering the time series $\eta(t_j) = \eta_{i^*j}$ associated with the series of earthquakes $j$ that occurred at time $t_j$ within the study area. The scaling parameters necessary for the computation of nearest neighbour distances $\eta_{ij}$, namely the *b-value* and the epicentres fractal dimension $\overline{d_f}$, are determined as the average values over the investigated area and time interval. Specifically, the *b-value* was set to b = 0.76, and the fractal dimension $\overline{d_f} = 0.90$, according to the median of the running average values of the parameters, estimated within the investigated area and time interval (see Fig. 7a and b). Fig. 7c shows the temporal variations of the nearest-neighbour distances $\eta$, between events in the Tolmezzo area from 2015 to March 2020.

The analysis shows that the most energetic events, E2 and E3, are associated with a relative minimum of the running average value of distance $\eta$. As a rule, the $\eta$ distance values keep relatively low after such events, due to the presence of several possible aftershocks, which are highly correlated. However, we observe that within several months (i.e., 5–10 months), the average distance $\eta$ has values similar to those preceding the main events. Hence, such earthquakes did not cause a substantial change in the long term in the investigated system, which progressively recovered its earlier state after the primary sequences induced by the E2 and E3 events.

## 6. Principal component analysis

### 6.1. Procedure

The principal component analysis (PCA), also known as principal parameters method (PPM), Empirical Orthogonal Functions (EOF) method, or Karhunen-Loève Transform, is a powerful technique for the analysis of the variability in geophysical fields through the first (centroid), and second moments (variance) of the data, and the Singular Value Decomposition. Hence, we can describe an $n$-dimensional data set through $m$ orthogonal functions ($m < n$), accounting for the data set variance.

Its application in seismology derived from interpreting the plane normal to the most minor axis of the correlation ellipsoid as the best fitting plane to a system of points (Pearson, 1901), i.e., the hypocentres: the length of the minimum axis is proportional to the mean square residual. In particular, it was used to infer the orientation of planes – of which the minimum axes is the pole - within seismic sequences, by sliding a fixed-width time-window along the sequence of seismic aftershocks by Ebblin and Michelini (1986); Michelini and Bolt (1986); Tselentis et al. (1989); Rossi and Ebblin (1990); Bressan et al. (2018b), or background seismicity (Bressan et al., 2016). The other two axes indicate the major and minor extents of the best-fit plane, respectively. Here, we used the multidimensional approach introduced by Rossi and Ebblin (1990), in which the time adds to the spatial coordinates in the construction of the 4D-correlation matrix, which can be interpreted as a hyper-ellipsoid. The hyper-ellipsoid spatial axes projection onto a 3-D space depicts the best-fit plane orientation, as for the 3-D case. The minimum axis is again normal to the plane that best fits the spatial distribution of the hypocentres, whereas the other two axes indicate the extent of the volume interested by the aftershocks. The fourth axis projection onto space indicates the propagation direction and can be used to infer the relationships between the various planes that activate in time (Rossi and Ebblin, 1990).

The elements of the matrix $C = [c_{ij}]$ are defined as

$$c_{ij} = c_{ji} = N^{-1} \sum_{k=1}^{k=N} \left( x_{ki} - \overline{x}_i \right) \left( x_{kj} - \overline{x}_j \right) \quad (5)$$

where $N$ is the earthquake number, $x_{k_i}$ and $x_{kj}$ are the hypocentre-coordinates in the $m$-dimensional space, for $i,j = 1,..,m$ and

$$\overline{x}_i = N^{-1} \sum_{k=1}^{k=N} x_{ki} \quad (6)$$

for $i = 1,..,m$ are the coordinates of the centroid. In our case, $m = 4$ and the coordinates are the three spatial coordinates and the occurrence time. Each dimension (spatial coordinates and time) is normalized for the difference between the maximum and minimum value of the spatial and time dimensions in the whole dataset, obtaining a-dimensional quantities.

The matrix $C$ can be viewed as an $m$-dimensional hyper-ellipsoid. The Singular Value Decomposition provides the principal semi-axes length from the eigenvalue square roots $T_i$ of the matrix $C$, with $i = 1,..,m$, and their orientation from its eigenvectors $u_{i,j}$ $(i,j = 1, \ldots,m)$. The analysis of the eigenvectors and the directional cosines enables us to easily distinguish the principal axis related to the time axis, correctly interpreting the results.

Following Pearson (1901) and Bressan et al. (2016), we define the

mean square residual (*SR*) from the best-fit plane as:

$$SR = \sqrt{\Delta} \bullet \mathrm{T}_{\min} \tag{7}$$

where Δ is the matrix determinant, and $T_{min}$ is the ellipsoid's minimum axis. It can be used as the criterion to choose the optimal size of the window used to analyze a hypocentre series, like that one, for which the *SR* values start to decrease, indicating that the plane best fits the distribution of the events considered.

Once we established a window size, we used further criteria to check the planarity of the solution and avoid including in the analysis solutions proper of a hypersphere. The first criterion is based on the ratio between the spatial eigenvectors; in particular we discard the solutions with $T_{max}/T_{min} < 2.5$ and $T_{med}/T_{min} < 1.75$ (Michelini and Bolt, 1986). The other criterion suggested by Rossi and Ebblin (1990) is based on the matrix's invariants $I_i$:

$$\begin{aligned} I_1 &= T_1 + T_2 + T_3 + T_4 \\ I_2 &= T_1 \bullet \; T_2 + T_2 \bullet T_3 + T_3 \bullet \mathrm{T}_4 + \mathrm{T}_1 \bullet \mathrm{T}_3 + \mathrm{T}_1 \bullet \mathrm{T}_4 + \mathrm{T}_2 \bullet \mathrm{T}_4 \mathrm{I}_3 \\ &= \mathrm{T}_1 \bullet \mathrm{T}_2 \bullet \mathrm{T}_3 + \mathrm{T}_2 \bullet \mathrm{T}_3 \bullet \mathrm{T}_4 + \mathrm{T}_1 \bullet \mathrm{T}_2 \bullet \mathrm{T}_4 + \mathrm{T}_1 \bullet \mathrm{T}_3 \bullet \mathrm{T}_4 \mathrm{I}_4 = \mathrm{T}_1 \bullet \mathrm{T}_2 \bullet \mathrm{T}_3 \bullet \mathrm{T}_4 \end{aligned} \tag{8}$$

where $T_i$ are the eigenvalues of the matrix. $I_4$ is proportional to the hypervolume of the hyperellipsoid, whereas $I_2$ *and* $I_3$, proportional to the sums of the elliptical and ellipsoidal sections of the hyperellipsoid, give a measure of their roundness.

The quantity $R_4$

$$R_4 = (I_2 \bullet \mathrm{I}_3)/(\mathrm{I}_1 \bullet \mathrm{I}_4) \tag{9}$$

is, therefore, a measure of the degree of flattening of the hyperellipsoid, being 6 in the case of a hypersphere and up to inifinity in the case of an infinitely flattened or elongated 4D hyperellipsoid (Rossi and Ebblin, 1990). Hence, in the following, we discard hyperellipsoids with $R_4 < 8$.

As pointed out by Bressan et al. (2016), in the case of the background seismicity, the best-fit plane of the hypocentre distribution is the mean or most representative orientation, while the minor axis, normal to it, and with length proportional to the mean square residual, can be seen as the thickness of the faulted and damaged zone.

Fig. 9 helps to understand the meaning of the fourth axis, namely the time axis, with a simple 2D example: the two dimensions are longitude and time. The colours progressively darker indicate increasing time.

In the case depicted in Fig. 9a, the shocks are clustered, with limited variation in the *E*-W direction with time. The major ellipse-axis coincides with the time axis. In Fig. 9b, the shocks show an evident propagation from West to the East, the major ellipse- axis forms an angle with the time-coordinate axis, and its projection on the EW axis would indicate the propagation direction.

To better explain and clarify the meaning of the various axes in a more complicated case, we built three different synthetic catalogues, the epicentral distribution of which is shown in Fig. 10a, c, e. In all three cases, the events (circles) are contained in a plane, EW oriented, and gently northwards dipping. The width of the circle is proportional to the event's depth (positive downwards). The number associated with the circle indicates the order with which the events occur in time. The analysis is performed considering all the events, i.e., 36 for the regular case of (a), 16 for (c) and 17 for (e). The results for the regular case of (a) are shown in (b). The maximum axis (yellow square) is EW oriented, the intermediate is northwards (green triangle), and so is also the time-axis projection (red circle). The blue diamond indicates the minimum spatial axis, interpreted as the pole of the fracturing plane (black line).

In the second experiment, we selected some of the events, following an oblique propagation, as whence several parallel fractures would be activated in sequence, succeeding to each other in SE-NW direction (c). In fact, in (d) the plane is the same (as expected), the maximum spatial axis indicates the direction of the fracturing lines, whereas the time axis (red circle) indicates NW, hence the direction of the general

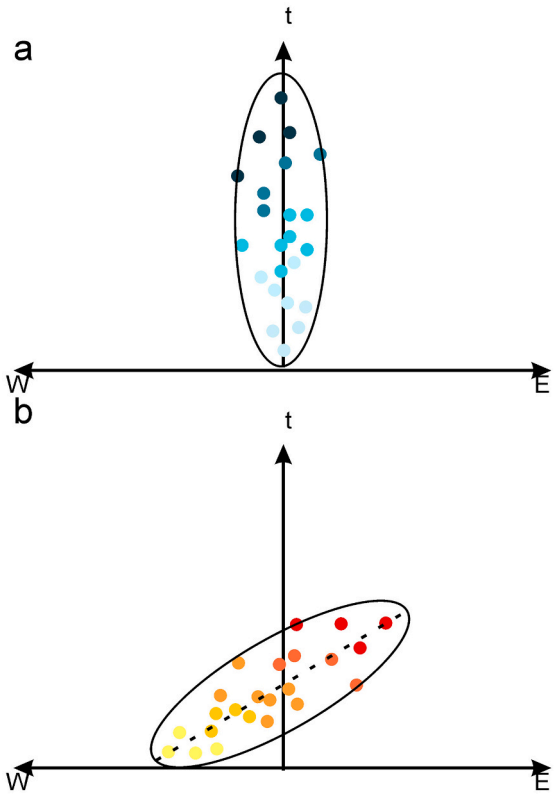


**Fig. 9.** Two-dimensional longitude-time example of principal component analysis (PCA). a) The shock distribution (dots from fair to dark blue, with darkness increasing with time) has a very limited spreading in longitude, and the distribution in time of the shocks is random. The major axis of an ellipse fitting the point's cloud is parallel to the time axis. b) The shock distribution (dots from yellow to red, yellow indicating the smallest, red the largest time) shows an evident propagation with time from W to E (the colour is progressively darker from West to East). The major axis of an ellipse fitting the point's cloud forms an angle to the time coordinate axis, pointing eastwards. (For interpretation of the references to colour in this figure legend, the reader is referred to the web version of this article.)

propagation. The third test (e) shows the activation of "patches", from the NE corner (and maximum depth) to the shallower part in the SW corner. The solution of (f) shows the major and intermediate spatial axes indicating the directions of the extension of the points in the space, whereas the time axis projection indicates the NE-SW direction of "activation" of the patches. We use a hollow red circle as a symbol, since we plot the projection on the lower hemisphere, but the verse of the time axis would be upwards and toward SW. Hence, also in the following, a hollow symbol for the time-axis projection will indicate propagation upwards.

Since we do not limit our analysis to the seismic sequences, and hence also a portion of background seismicity is included, the minimum spatial axis is the pole of the best-fit plane, i.e., the fracturing plane. The maximum and intermediate spatial axes indicate the directions along which the fracturing is propagating, and, hence, the extent of the fracturing zone. The time-axis projection on the space volume indicates the general/total propagation direction (Table 1).

With these premises, the time-axis projection on the space volume, compared with the other axes geometry, can help understanding the seismicity evolution. If the time-axis projection lies in the best-fit plane, it indicates the fracture propagation direction, close to the fracture borders (coinciding with the maximum axis), or along anisotropy or weakness lines. On the contrary, if the time-axis projection lies close to the best-fit plane pole (the most minor spatial axis), it indicates that the fracturing propagates on planes parallel to the best-fit one. If it lays in

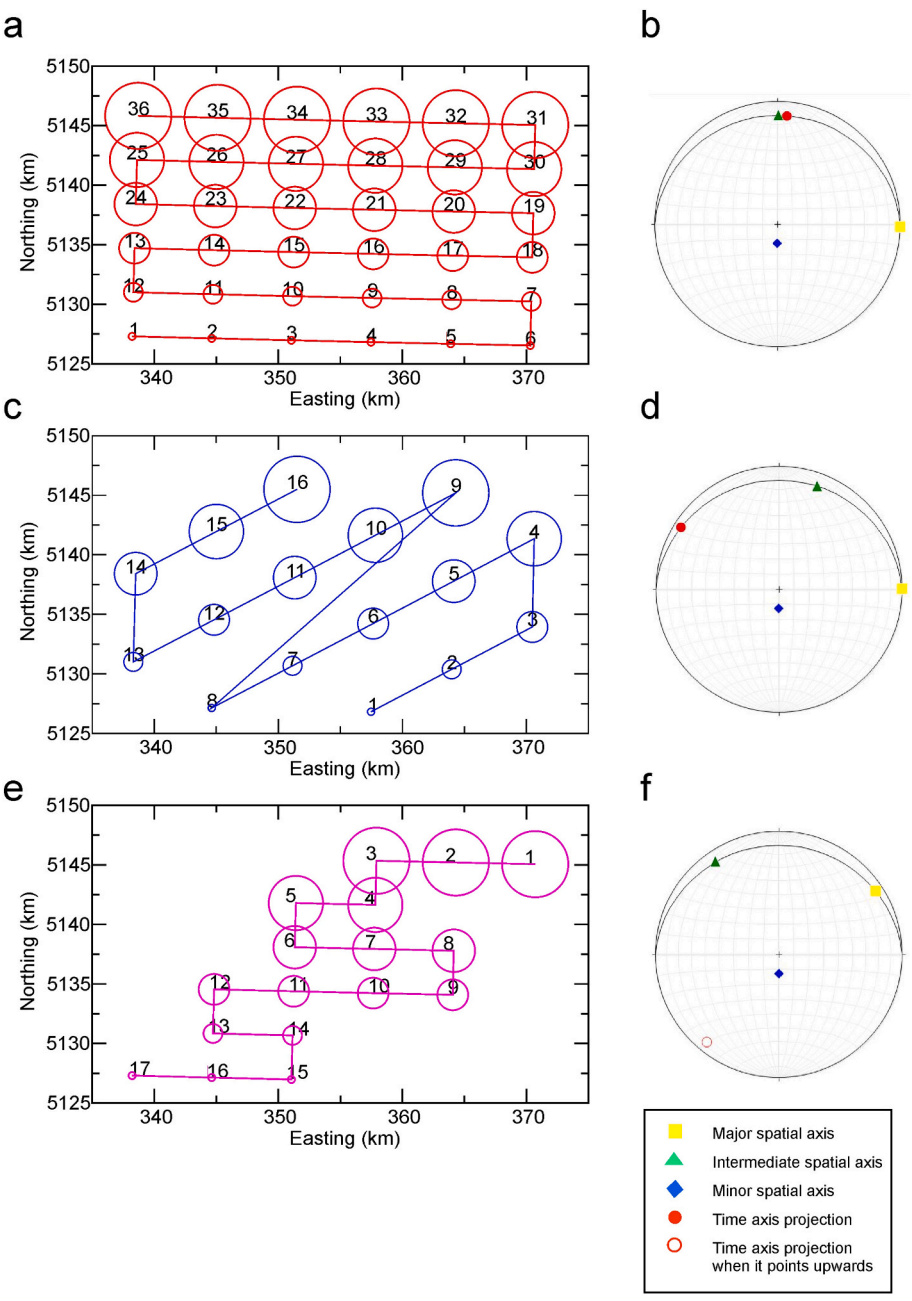


**Fig. 10.** Synthetic cases and PCA analysis. a), c), e): plan view of the synthetic events (circles); in all cases, the foci are contained in a plane, EW oriented, and gently dipping to the north: the size of the circle is proportional to the depth of the event (positive downwards). The number associated with the circle indicates the order of the time-sequence. a) regular case, 36 events; c) the 16 events are distributed along several parallel lines NE-SW oriented, activated from SE to NW. e) the 17 events are contained into three "patches," progressively activated from NE to SW and from the depth to the surface. b), d), f): results of the PCA analysis of the data in a), c), e). Stereographic projection (lower hemisphere) with the projection of the hyperellipsoid's four axes. Yellow box: spatial major axis; green triangle: spatial intermediate axis; blue diamond: spatial minor axis, or pole of the plane; the black line is the plane, normal to the spatial minor axis. Red circle: time-axis projection on the 3D space: if hollow, it indicates the upwards verse of the propagation. (For interpretation of the references to colour in this figure legend, the reader is referred to the web version of this article.)

**Table 1**
Interpretation scheme of the 4-D hyperellipsoid axes of the correlation matrix.

| Hyperellipsoid axis | Directions |
|---|---|
| Spatial minimum axis (blue diamond) | Normal to the best-fit plane- thickness of the fractured zone |
| Spatial intermediate axis (green triangle) | Minor extent of the fracturing zone |
| Spatial maximum axis (yellow square) | Maximum extent of the fracturing zone |
| Time axis (red dot: if hollow, upwards propagation) | Propagation direction |

the plane containing the two smallest spatial axes, this indicates an out-of-plane propagation. For dip-slip mechanisms, such geometry can indicate curvature of the plane, as, e.g., in the case of listric faults. In a strike-slip framework, the same time-axis relative position can mean the activation of a different order of planes, as in the case of an en-echelon system: the time-axis indicates the direction in which the faults are progressively activated. Finally, suppose time-axis projection is contained in the plane containing the maximum and minimum axis or is in a different direction not directly correlated with the other axes, we deduce that different fracturing planes or clusters are activated, respectively.

## 7. Results

The PCA analysis was performed considering time-successive groups of seismic hypocentres by sliding a time-window of a fixed earthquake-number along the events time-series. We calculated the mean square residual (*SR*) of the best fitting plane as a function of the window size, measured in terms of the number of events included in it (eq. 7; Fig. 11). Increasing the window size (and hence the number of events), the *SR* initially increases, then, for a size larger than 25 events, it decreases, indicating that the plane best fits the distribution of the events included in the analysis. Accordingly, we chose the window size for which the *SR*

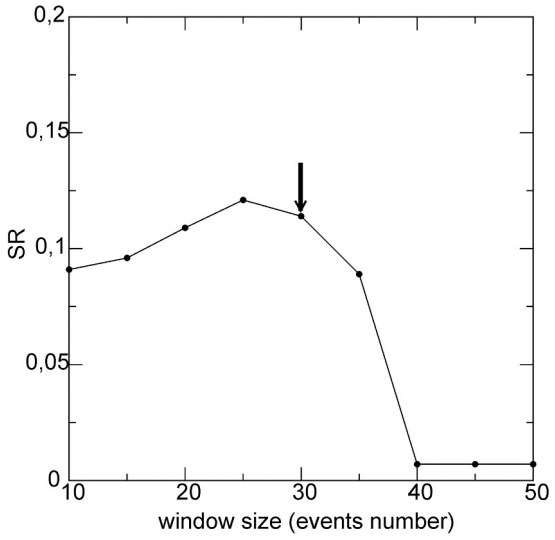


**Fig. 11.** Variation of the mean square residual (SR) of the ipocentres distribution from the best-fit plane with the increase in window size, as measured by the number of included events. The arrow marks the window size chosen for the subsequent analyses.

started to decrease markedly, which corresponds to $N = 30$ events. The analysis was carried out along the geological cross-section of Fig. 2 on three spatial windows (Fig. 12a) of about 10 km in longitude and 6.7 km in latitude, from 12.96E, 46.31 N to 13.09E, 46.49 N, i.e., to the south of the Tolmezzo town, centred on it and to the north of it. The southern zone (zone 1) is centred on the E2 event, the second (zone 2) hosts E1 and E3, whereas the third (zone 3) hosts E4.

Fig. 12 shows the stereograms with the ellipsoid axes directions and the planes normal to the minimum spatial axis. As above said, to guarantee to consider only those foci distributions that could be effectively represented by more or less planar distributions of earthquakes, we discarded the hyperellipsoids with $T_{max}/T_{min} < 2.5$ and $T_{med}/T_{min} < 1.75$ and the ones with $R_4 < 8$.

The first zone epicentres distribution evidences the marked clustering bound to the E2 event (Fig. 12a). The maximum fracturing extension is vertical as most of the time-axis projection (Fig. 12b). The best fit planes are from sub-vertical to vertical, NW-SE oriented from 2015 to the end of 2017, and NNE-SSW during 2018 and 2019. During this last period, the time axis projection, pointing upwards, first is close to the intermediate axis, revealing the extension of fracturing in that direction, and then it is contained in the fracturing planes, indicating NW-SE, sub-vertical as the direction of possible weakness or anisotropy.

As regards as the epicenter pattern of zone 2, which includes the E1 and E3 events and sequences, although widely distributed, it shows an apparently dominant ENE-WSW distribution (Fig. 12a). The PCA solutions (Fig. 12c) are two sets of vertical planes: the first, WNW-ESE trending, activated in 2015 and then reactivated in the first months of 2018. The second is ENE-WSW trending and characterizes the seismic activity of 2017. Interestingly, the time axis projection is about constant in N128W direction until the E4 event, mainly upwards, but with variable dip, steeper for the ENE-WSW solutions. According to the scheme of Table 2, it can be interpreted as the direction of the fracture propagation and possibly activation of new clusters. In the last months of 2019, although the spatial axes remain fixed, indicating planes WNW-ESE trending, the time axis projection moves southwards, close to the pole, indicating a southwards propagation and the activation of parallel planes. Then, it rotates to N135W, which will be the orientation of the

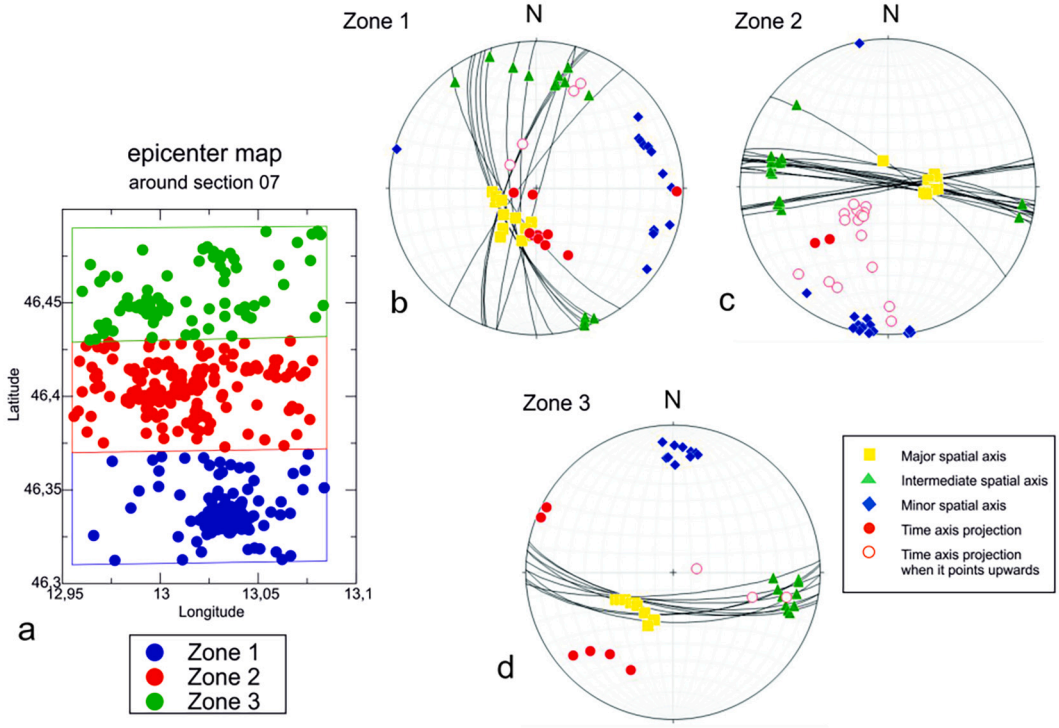


**Fig. 12.** a) distribution of the epicentres of the events with $M_C = 1$ of the catalogue, in the region 10 km wide, centred on the section A-B of Fig. 1, in three spatial windows of about 10 km in longitude and 6.7 km in latitude. The circles are the epicentres of the earthquakes analyzed with PCA: bluecircles: zone 1; red circles: zone 2; green circles: zone 3. b) PCA solutions obtained by sliding a 30 events window along the events in the zone 1; c) PCA solutions obtained by sliding a 30 events window along the events in the zone 2; d) PCA solutions obtained by sliding a 30 events window along the events in the zone 3. Yellow square: Maximum spatial axis; green triangle: intermediate spatial axis; blue diamond: minimum space axis; red dot: time axis projection on the space volume: if hollow, the verse is upwards. Black lines:planes normal to the spatial minor axes (blue diamond). (For interpretation of the references to colour in this figure legend, the reader is referred to the web version of this article.)

**Table 2**
Interpretation scheme of the 4D hyperellipsoid time-axis projection onto the 3D space.

| Time-axis location | Interpretation | Time-axis direction meaning |
|---|---|---|
| In the best-fit plane | The shock distribution is close to a plane | Anisotropy or weakness lines. |
| Close to the maximum or intermediate spatial axes | The fracture is extending | Fracturing area borders |
| Close to the best-fit plane pole (minimum axis) | The fracturing propagates normally to the best-fit plane. | Direction of the planes parallel to the best-fit one |
| In the plane containing the two smallest spatial axes | Out-of-plane rupture. Dip-slip: plane curvature; strike-slip: en-echelon system. | Direction of fracturing extension |
| On the plane containing the maximum and minimum spatial axes | Activation of different planes | Direction of the new planes |
| Not closely aligned with any of the spatial axes and planes | Passage from one cluster to another one | Direction of the fracture propagation/ new clusters |

pole of the plane best fitting the earthquakes that occurred between 2019 and 2020. Zone 3 is characterized by fewer events, and it is evident the clustering related to the E4 event (Fig. 12a). Whereas the orientation of the three spatial axes is about constant, with small oscillations around a solution implying a plane about EW oriented, 60–75° southwards dipping, the time axis moves gradually from a direction N150W, indicating the fracture propagation and possibly activation of new clusters, to directions N75W, first sub-horizontal and then steeper, while the axis turn upwards, close to the best-fit plane (Fig. 12d).

## 8. Discussion

The multi-parametric analysis reveals a complex temporal evolution of the seismicity in the examined area.

Oscillations characterize the normalized Shannon entropy temporal variation (Fig. 6), with temporary local drops caused by clusters of higher radiated seismic energy. The most significant decreases are associated with $M_D \geq 3.7$ mainshocks and their aftershocks. After the last episode of the E4 earthquake, the entropy recovers to the level preceding the seismic sequences.

The *b-value* temporal variation is characterized by a positive trend until mid-2017 and, afterwards, it shows significant fluctuations from about 1.2–1.4 to 0.5 (Fig. 7a). Specifically, the *b-value* decreases from about 18 weeks to 5 weeks before the E1, E2, E3 largest earthquakes occurred close to Tolmezzo. The fractal dimension time-variation (Fig. 7b) reveals fluctuations with marked decreases in correspondence of the sequences E2, E3. The temporal pattern of $\eta$ (Fig. 7c) is characterized by low values corresponding to the sequences associated with the most severe shocks and clusters of minor swarms. The running average trend is nearly constant up to August 2018, when the E2 earthquake occurs, and then it is characterized by broader fluctuations.

The PCA analysis (Fig. 12) of the seismicity in the three zones along the geological cross -section of Fig. 2 reveals two distinct temporal phases in the zones 1 and 2 (containing E2, and E1 and E3 events sequences, respectively). During 2015–2017, the best-fit planes are sub-vertical and trending NW-SE in zone 1, whereas they are vertical, and ENE-WSW oriented in zone 2. The fracturing tends to propagate vertically in zone 1, whereas along N128W direction in zone 2. The next phase (2018–2020) is characterized by sub-vertical NNE-SSW oriented planes for the zone 1, and WNW-ESE vertical planes for zone 2. The fracture propagates for zone 1 mainly within the fracturing plane, along directions of weakness about NW-SE, whereas for zone 2, the time-axis projection indicates the activation of parallel planes. Toward the end of the period considered, in the first months of 2020, it moves to a new direction (N135W), which also becomes the pole of a new best-fit plane of the hypocentral distribution, sub-vertical, northwards dipping, N60W oriented. The seismicity of zone 3, which includes the E4 sequence, is best represented by the same plane throughout the whole period, i.e., a steep about EW oriented plane, 60–75° southwards dipping. Also in this case, the fracturing propagates in a direction close to the one observed for zone 2 (N150W) and in the fracturing plane, along weakness lines.

The damage pattern outlined in the vertical cross-section of Fig. 5 suggests that the distribution of seismicity is closely related to the heterogeneities of the involved materials. The seismicity appears mainly distributed in correspondence of the sharp transitions from zones characterized by low damage (0.1), consistent with high in-situ shear modulus, to zones with intermediate damage (0.35), consistent with lower in-situ shear modulus (Bressan et al., 2012). This pattern supports the argument that the zones of marked variation of the elastic moduli are most favourable to the localization of fractures in a mechanically heterogeneous medium subject to a stress field. From a scale-invariant perspective of the process, this agrees with the heterogeneous rocks under loading observed in laboratory tests. Liu (2003) found that the grain boundaries in crystalline heterogeneous materials are the predominant source of stress concentrating cracks.

De Franco et al. (2004) considered the in-situ shear modulus as a function of the state of damage of the crustal rocks. The authors proposed that the magnitude of the rock-strength gradient correlates with the seismic energy and that the second spatial derivative is negatively correlated to the radiated seismic energy. According to this proposed model, lower shear-modulus zones, pertaining to less competent rocks, are characterized by more frequent and low seismic-energy events than higher shear-modulus zones.

The damage pattern and the temporal variations of the parameters that we used for describing the features of seismicity lead to an interpretation based on the key role played by the mechanical heterogeneity of the upper crust on the space-time distribution of seismicity. The local strain induced by applied remote tectonic stress is variable because of the non-uniform deformation of the heterogeneous rocks. The process is time-dependent because stresses and deformations are continuously redistributed until the brittle failure occurs, depending on the different strength thresholds of rocks. According to this view, rock behaviour depends on the history of the past deformation. The process results in temporal fluctuations of the local strain energy and, therefore, of the seismic activity.

The Shannon entropy temporal evolution (Fig. 6) is characterized by fluctuations around a nearly constant level and drops, clusters of higher radiated seismic energy, more markedly in correspondence of the seismic sequences. By recalling the Shannon entropy's meaning, the time sequence mainshock-aftershocks characterizes the maximum information and the maximum spatial organization of the analyzed system, with a consequent entropy value decrease.

In our interpretation, the drop of the Shannon entropy and fractal dimension indicates damage localization.

The *b-value* was characterized during the period 2017–2019 by relevant temporal fluctuations (Fig. 7a). The temporal variation of *b-values* can be related to crustal stress changes. Scholz (1968) found from laboratory measurements that the temporal variation of b is related to differential stress, with a negative correlation between the *b-values* and the stress level. Schorlemmer and Wiemer (2005) claimed that the spatial and temporal variation of *b-value* could be considered a stress-meter, and low *b-values* can be attributed to highly stressed patches in the fault. Goebel et al. (2012) analyzed acoustic emissions on Westerly granite samples, with and without notches, under triaxial compressions. They found that spatial *b-value* anomalies and seismic clusters are linked to the fault zone's heterogeneity and are directly connected to the asperity zones. Accordingly, lower *b-values* can be associated with highly stressed asperities, which well explains the low values of *b* estimated prior to the main events in the study area (Fig. 7a).

The effect of heterogeneity of the fault or rock mass on event-rates, *b-values,* and fractal dimension has been emphasized by Lei et al. (2004),

who presented detailed laboratory experimental results of acoustic emissions of catastrophic fracture of rock samples under triaxial compression. The samples contain a pre-existing fault of widely different strength and are characterized by different mechanical properties. Lei et al. (2004) found that the temporal evolution of the *b-value* and fractal dimension depends on the degree of the samples heterogeneity. In particular, the stress enhancement is favoured at the boundaries of the asperities, favouring damage localization and explaining the temporal fluctuations of the *b-value*. On the other hand, the fractal dimension decreases are meaningful in the case of pre-existing fracture plane modeled by heterogeneous healing strength.

Following Goebel et al. (2013), who investigated the temporal pattern of the acoustic emissions on samples in triaxial experiments, we interpret the fluctuations of *b-value* (Fig. 7a) as indicators of stress. Accordingly, the *b-value* drops before the most significant earthquakes are related to increasing stresses, while the *b-value* rises associated with the aftershock sequences can be related to decreasing stress. In particular, we observed a noticeable decrease of the *b-value* from about 18 weeks to 5 weeks before the E1, E2, E3 earthquakes occurred in the study area, close to Tolmezzo.

The fractal dimension time-variation is characterized by fluctuations around 0.9 with a peak at 1.25 and a minimum around 0.1. The mean value is indicative of a distribution tending to linearity. The minimal/smallest values correspond to the clustering of weak seismicity and aftershock sequences except for E1, which is characterized by few aftershocks with low radiated seismic energy. This aspect has been explained by Bressan et al. (2007) with the stress release mechanism of the mainshock. They found that the partitioning of the radiated seismic energy between the mainshock and the aftershocks depends on the mainshock's Brune stress drop. Fig. 13 shows the Brune stress drop of the mainshock related to the ratio $R_{ES}$ between the energy radiated by the mainshock and total amount of the radiated energy by the aftershocks of the most well-documented seismic sequences occurred in the Friuli-Slovenia areas in the last years (Bressan et al., 2017), updated with the sequences considered in this study. The ratio $R_{ES}$ increases with the increasing Brune stress drop.

The damage evolution and the radiated seismic energy was modeled by Tang and Kaiser (1998) with a compressive loading test on heterogeneous rock samples. The degree of mechanical heterogeneity influences the damage evolution and the occurrence of seismicity. In particular, the clustering of seismicity is favoured by weak mechanical zones included in the sample, and the most significant energy release corresponds to the failure of high strength zones.

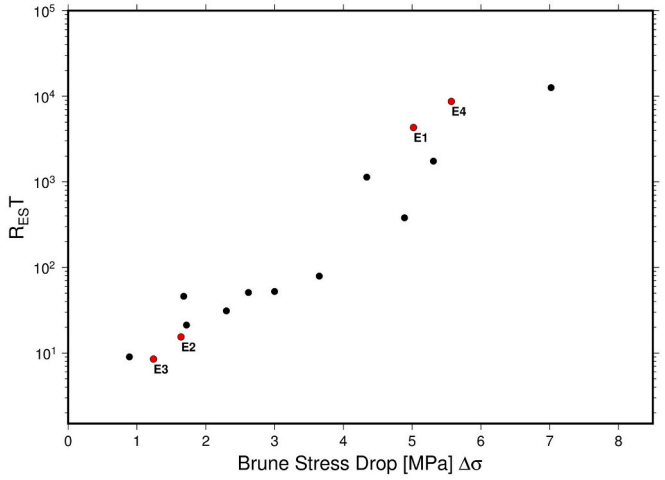


**Fig. 13.** Brune stress drop versus the ratio between the energy radiated by the mainshock and the summation of the energies radiated by the aftershocks ($R_{ES}$) of most important seismic sequences occurred in the Friuli-Slovenia areas (modified from Bressan et al., 2017). The data of Bressan et al. (2017), reported as black dots, have been updated with the seismic sequences of E1, E2, E3, E4 (red dots). (For interpretation of the references to colour in this figure legend, the reader is referred to the web version of this article.)

Here, the temporal variation of clustering properties of the earthquake population has been furthermore investigated through the parameter $\eta$ (Fig. 7c). We recall that $\eta$ analyzes the distance between two earthquakes that are not consecutive events but rather the nearest neighbour events, namely the most correlated seismic events, with a minimum η distance in the space-time-energy domain. Ren et al. (2019) analyzed the acoustic emissions on concrete beams under uniaxial compression. They found that the decreases of the nearest neighbours distance $\eta$ is correlated with decreases of the *b-value* and fractal dimension.

Under remote loading, the damage in heterogeneous rocks changes with time because of the strain energy redistribution; its behaviour depends on its previous history and is reflected in the temporal evolution of seismicity clusters. Therefore, the parameter $\eta$ can be considered a parameter related to the "memory" of past deformations.

The PCA solutions (Fig. 12) reveal mostly vertical and sub-vertical planes fitting the seismicity, changing orientation along the geological cross-section. The fracture propagates within the fracturing plane in the southernmost part of the cross-section (zone 1), with the activation of parallel planes in the central part (zone 2) and along weakness lines in the northern part (zone 3). The orientation of the planes inferred from PCA analysis differs from the orientation of the major faults recognized in the area (Fig. 1 and Fig. 2), although NNE-SSW and E-W trends have been recognized in the region considered. The best-fit planes derived from PCA analysis and the fault plane solutions of the main shocks show a weak similarity, overall in the dip. The focal mechanisms were computed from P-wave first polarity. The differences can be due to the assumption of plane surface of the seismic source. The focal planes can be different if the early asperity that yields is not coplanar with the mean orientation of the rupture surface. Moreover, the PCA analysis is performed on catalogues including the four sequences, but not limiting the analysis to them, and, therefore, the solutions are relative to more fracturing features.

These results support the concept that the time evolution of the seismicity has to be considered within the context of damage and localization of deformations, depending on the coupling between applied remote tectonic stress and the mechanical rock heterogeneities. In fact, the change in orientation of the best fitting planes and of the fracture propagations are accompanied by relevant fluctuations of the *b-value*, $\eta$ parameter, and fractal dimension. Ma et al. (2011)'s results support this view. They investigated the fracture pattern with a method simulating the heterogeneous rock-like material behaviour under uniaxial and biaxial compressive loading. The failure pattern evolution was modeled by an elastoplastic damage model and a Weibull distribution of elastic parameters characterizing the heterogeneity. The simulation evidenced that the failure pattern evolves with time. They found that the larger is the mechanical heterogeneity, the more complex the failure pattern becomes, with a different orientation of the failure planes.

## 9. Conclusions

The multi-disciplinary approach proposed here allowed us to describe in a quantitative way the seismicity evolution in time and in space, distinguishing different phases and interpreting them as the expression of progressive damage of the crustal rocks, which rules the hypocentres pattern and fracturing propagation.

The study area is located in NE Italy, centred on the town of Tolmezzo, and is of high interest for the complex tectonics, and moderate seismic activity. Two distinct periods of the temporal evolution of seismicity are identified, as revealed by the *b-value* and the fractal dimension, which show relevant fluctuations since the beginning of 2017. The temporal variation of the *b-value* can be related to crustal stress changes in a medium characterized by different mechanical properties. The

fractal dimension time evolution indicates a prevailing clustering of the earthquakes with a tendency to propagate linearly. The temporal variations of the Shannon entropy and $\eta$ quantify the evolving organization and correlation of seismicity within an area; hence, they reflect a process of damage evolution in heterogeneous rocks that changes with time due to continuous strain energy redistribution. According to this view, the Shannon entropy and $\eta$ can be considered as parameters related to each other that reflect the memory of past deformations. The recovery of Shannon entropy and $\eta$ to values preceding the crisis of 2018–2019 suggests that the system has reached a temporary new equilibrium.

These issues are also reflected in the temporal variation of the direction of the fracture propagation and the orientation of the planes fitting the earthquake foci close to the Tolmezzo town.

We recall that the study area, especially the central part around the Tolmezzo municipality, particularly from 6 to about 12 km depth, is characterized by a complex tectonic pattern, resulting by the maximum interference between the NW-SE oriented Dinaric overthrusts and the E-W trending Alpine thrusts and backthrusts. The fault geometry is complex and involves large volumes of deformation with zones of variable fracture frequency and extent, and multiple anastomosing branches. Furthermore, the rocks involved are mechanically heterogeneous, with a wide range of shear modulus values, as revealed by earlier seismo-gravimetric tomographic images.

Under these conditions, the spatial distribution of seismicity is not uniform, but it is characterized by local clusters, as revealed by the fractal analysis and planes changing orientation with time, detected with the PCA method. Therefore, the stress concentrations and the localization of seismicity appear to be controlled by the geometric interaction between faults and by sharp variations of rock mechanical characters. Although performed on a limited area, the adopted procedures and the resulting observations can be applied to other areas of complex tectonics to investigate the time-evolution of the seismicity and the damage.

## Declaration of Competing Interest

None.

## Acknowledgments

We are grateful to the two anonymous reviewers for their valuable comments, which allowed us to improve the manuscript. The authors thank S. Urban and A. Magrin for help in graphics and critical reading of the manuscript. The local seismic network is managed by the Seismological Research Centre of the National Institute of Oceanography and Applied Geophysics – OGS with the financial contribution of the Regione Friuli Venezia Giulia.

## References

Aki, K., 1965. Maximum likelihood estimate of b in the formula logN=a-bM and its confidence limits. Bull. Earthquake Res Inst. Tokyo Univ. 43, 237–239.
Anderson, H., Jackson, J., 1987. Active tectonics of the Adriatic region. Geophys. J. R. Astron. Soc. 91, 937–983.
Baiesi, M., Paczuski, M., 2004. Scale-free networks of earthquakes and aftershocks. Phys. Rev. E 69, 066106. https://doi.org/10.1103/PhysRevE.69.066106.
Barnaba, C., Marello, L., Vuan, A., Palmieri, F., Romanelli, M., Priolo, E., Braitenberg, C., 2010. The buried shape of an alpine valley from gravity surveys, seismic and ambient noise analysis. Geophys. J. Int. 80 (2), 715–733. https://doi.org/10.1111/j.1365-246X.2009.04428.x.
Benali, A., Peresan, A., Varini, E., Talbi, A., 2020. Modelling background seismicity components identified by nearest neighbour and stochastic declustering approaches: the case of northeastern Italy. Stoch. Env. Res. Risk A. 34, 775–791. https://doi.org/10.1007/s00477-020-01798-w.
Ben-Zion, Y., 2001. Dynamic ruptures in recent models of earthquake faults. J.Mech. Phys. Solids 49, 2209–2244.
Ben-Zion, Y., Sammis, C.G., 2003. Characterization of fault zones. Pure Appl. Geophys. 160, 677–715.
Bressan, G., Kravanja, S., Franceschina, G., 2007. Source parameters and stress release of seismic sequences occurred in the Friuli-Venezia Giulia region (northeastern Italy) and in western Slovenia. Phys. Earth Planet. Int. 160, 192–214. https://doi.org/10.1016/j.pepi.2006.10.005.
Bressan, G., Gentile, G.F., Tondi, R., de Franco, R., Urban, S., 2012. Sequential integrated inversion of tomographic images and gravity data: an application to the Friuli area (north-eastern Italy). Boll. Geof. Teor. Appl. 53, 191–212.
Bressan, G., Ponton, M., Rossi, G., Urban, S., 2016. Spatial organization of seismicity and fracture pattern in NE Italy and W Slovenia. J. of Seismology 20, 511–534. https://doi.org/10.1007/s10950-015-9541-9.
Bressan, G., Barnaba, C., Gentili, S., Rossi, G., 2017. Information entropy of earthquake populations in northeastern Italy and western Slovenia. Phys. Earth Planet. Inter. 271, 29–46. https://doi.org/10.1016/j.pepi.2017.08.001.
Bressan, G., Barnaba, C., Bragato, P., Ponton, M., Restivo, A., 2018a. Revised seismotectonic model of NE Italy and W Slovenia based on focal mechanism inversion. J. Seismol. 22, 1563–1578. https://doi.org/10.1007/s10950-018-9785-2.
Bressan, G., Barnaba, C., Magrin, A., Rossi, G., 2018b. A study on off-fault aftershock pattern at N-Adria microplate. J. Seismol. 22, 863–881. https://doi.org/10.1007/s10950-018-9737-x.
Carulli, G.B., 2000. Il nodo tettonico di Tolmezzo e la struttura del M. Amariana, in "Guida alle Escursioni", 80°Riunione Estiva della Società Geologica Italiana, Trieste, 6–8 settembre 2000.
Carulli, G.B., 2006. Carta Geologica del Friuli Venezia Giulia alla Scala 1:150.000—Note Illustative. S.E.L.C.A. Firenze, 2006, Italy.
Castellarin, A., Cantelli, L., 2000. Neo-Alpine evolution of the Southern Eastern Alps. J Geodynamics 30 (1–2), 251–274. https://doi.org/10.1016/S0264-3707(99)00036-8.
De Franco, R., Bressan, G., Gentile, G.F., 2004. Elastic moduli and seismogenic aspects of the Friuli upper crust. Boll. Geof. Teor. Appl. 45 (1–2), 71–87.
Ebblin, C., Michelini, A., 1986. A principal parameter analysis of aftershock sequences applied to the 1977 Friuli, Italy, sequence. Ann. Geophys. 4, 473–480.
Eneva, M., 1996. Effect of limited data sets in evaluating the scaling properties of spatially distributed data: an example from mining-induced seismic activity. Geophys. Journ. Int. 124, 773–786. https://doi.org/10.1111/j.1365-246X.1996.tb05637.x.
Faccenda, M., Bressan, G., Burlini, L., 2007. Seismic properties of the upper crust in the central Friuli area (northeastern Italy) based on petrophysical data. Tectonophysics 445, 210–226.
Goebel, T.H.W., Becker, T.W., Schorlemmer, D., Stanchits, S., Sammis, C., Rybacki, E., Dresen, G., 2012. Identify fault heterogeneity through mapping spatial anomalies in acoustic emission statistics. Journ. Geophys. Res. 117, B03310 https://doi.org/10.1029/2011JB008763.
Goebel, T.H.W., Schorlemmer Becker, T.W., Dresen Sammis, C.G., 2013. Acoustic emissions document stress changes over many seismic cycles in stick-slip experiments. Geophys. Res. Lett. 40, 2049–2054. https://doi.org/10.1002/grl.50507.
Grassberger, P., 1983. Generalized dimensions of strange attractors. Phys. Lett. 97A, 227–230.
Gutenberg, B., Richter, C.F., 1944. Frequency of earthquakes in California. Bull. Seismol. Soc. Am. 34, 185–188.
Havstad, J.W., Ehlers, C.L., 1989. Attractor dimension of nonstationary dynamical systems from small data sets. Phys. Rev. A 39, 845–853. https://doi.org/10.1103/physreva.39.845.
Hirata, T., Satoh, T., Ito, K., 1987. Fractal structure of the spatial distribution of microfracturing in rock. Geophys. J. R. Astron. Soc. 90, 369–374. https://doi.org/10.1111/j.1365-246X.1987.tb00732.x.
Kachanov, L.M., 1986. Introduction to Continuum Damage Mechanics. Martinus Nijhoff Publishers, Dordrecht, The Netherlands.
Kagan, Y.Y., 2007. Earthquake spatial distribution: the correlation dimension. Geophys. J. Int. 168, 1175–1194. https://doi.org/10.1111/j1365-246X.2006.03251x.
Krajcinovic, D., 1996. Damage Mechanics. Elsevier, Amsterdam (761 p).
Lei, X., Masuda, K., Nishizawa, O., Jouniaux, L., Liu, L., Ma, W., Satoh, T., Kusunose, K., 2004. Detailed analysis of acoustic emission activity during catastrophic fracture of faults in rock. J. Struct. Geol. 26, 247–258.
Liu, H.Y., 2003. Numerical modelling of the rock fracture process under mechanical loading. Licentiate thesis. Lulea University of Technology, p. 04.
Ma, G.W., Wang, X.J., Ren, F., 2011. Numerical simulation of compressive failure of heterogeneous rock-like materials using SPH method. Int. Journal of Rock Mechanics and Mining Sciences 48, 353–363.
Mandelbrot, B.B., 1977. Fractals: form, chance and dimensions. W.H. freeman, S. Francisco (365 pp).
Mantovani, E., Albarello, D., Tamburelli, C., Babbucci, D., 1996. Evolution of the Tyrrhenian basin and surrounding regions as a result of the Africa-Eurasia convergence. J. Geodyn. 21, 35–72.
Michelini, A., Bolt, B., 1986. Application of the principal parameters method to the Coalinga, California, aftershock sequence. Bull. Seis. Soc. Am. 76, 409–420.
Mignan, A., Woessner, J., 2012. Estimating the magnitude of completeness in earthquake catalogues. Community Online Resource for Statistical Seismicity Analysis. https://doi.org/10.5078/corssa-00180805. Available at. http://www.corssa.org.
Molchan, G., Kronrod, T., 2005. On the spatial scaling of seismicity rate. Geophys. J. Int. 162, 899–909. https://doi.org/10.1111/j1365–246X2005.02693x.
Pearson, K., 1901. On lines and Planes of closest fit to Systems of Points in space. Philos. Mag. 2, 559–572. https://doi.org/10.1080/14786440109462720.
Peresan, A., Gentili, S., 2018. Seismic clusters analysis in northeastern Italy by the nearest-neighbour approach. Phys. Earth. Plan. Int 274, 87–104. https://doi.org/10.1016/j.pepi.2017.11.007.

Poli, M.E., Zanferrari, A., 2018. The seismogenic sources of the 1976 Friuli earthquakes: a new seismotectonic model for the Friuli area. Boll. Geof. Teor. Appl. 59, 463–480. https://doi.org/10.4430/btga0209.

Ponton, M., 2010. Architettura delle Alpi Friulane. Museo Friulano di Storia Naturale 52, Udine (80 pp).

Ponton, M., 2015. Depth structural analysis of the external Dinaric chain in Julian Alps and Prealps (Italy and Slovenia). Gortania Atti Museo Friulano di St Nat Udine 36, 23–34.

Rebez, A., Renner, G., 1991. Duration magnitude for the northeastern Italy seismometric network. Boll. Geof.Teor. Appl. 33, 177–186.

Ren, D., Liu, B., Sun, J., Song, Y., Lin, Z., Liu, B., 2019. Interevent acoustic emission character of three-point-bending tests on concrete beams by the nearest neighbor distance. Constr. Build. Mater. 224, 359–371.

Rong, F., Wang, H., Xia, M., Ke, F., Bai, Y., 2006. Catastrophic rupture induced damage coalescence in heterogeneous brittle media. Pure Appl. Geophys. 163, 1847–1865.

Rossi, G., 1990. Fractal dimension time variations in the Friuli (northeastern Italy) seismic area. Boll. Geof. Teor. Appl. 32, 175–184.

Rossi, G., 1994. Fractal analysis as a tool to evidence seismic cycle phases. In: Kruhl, J.H. (Ed.), Fractals and Dynamic Systems in Geoscience. Springer-Verlag, Berlin Heidelberg., pp. 169–179

Rossi, G., Ebblin, C., 1990. Space (3-D) and space-time (4-D) analysis of aftershock sequences: the Friuli (ne Italy) case. Boll. Geof. Teor. Appl. 22, 37–49.

Rovida, A., Locati, M., Camassi, R., Lolli, B., Gasperini, P., 2016. CPTI15, the 2015 version of the parametric catalogue of Italian earthquakes. Istituto Nazionale di Geofisica e Vulcanologia. https://doi.org/10.6092/INGV.IT-CPTI15.

Scholz, C.H., 1968. The frequency-magnitude relation of microfracturing in rock and its relation to earthquakes. Bull. Seismol. Soc. Am. 58, 399–415.

Schorlemmer, D., Wiemer, S., 2005. Microseismicity data forecast rupture area. Nature 434, 1086. https://doi.org/10.1038/4341086a.

Shannon, C.E., 1948. A mathematical theory of communication. Bell Syst. Tech. J. 27 (379–423), 623–656.

Shi, Y., Bolt, B.A., 1982. The standard error of the magnitude- frequency b-value. Bull. Seismol. Soc. Am. 72, 1677–1687.

Slejko, D., Neri, G., Orozova, I., Renner, G., Wyss, M., 1999. Stress field in Friuli (NE Italy) from fault plane solutions of activity following the 1976 main shock. Bull. Seism. Soc. Am. 89, 1037–1052.

Tang, C.A., Kaiser, P.K., 1998. Numerical simulation of cumulative damage and seismic energy release during brittle rock failure-part I: fundamentals. Int. J. Rock Mech. Min. Sci. 35 (2), 113–121.

Telesca, L., Lapenna, V., Lovallo, M., 2004. Information entropy analysis of seismicity of umbria-marche region (Central Italy). Nat. Haz. Earth Syst. Sci. 4, 691–695.

Theiler, J., 1986. Spurious dimension from correlation algorithms applied to limited time-series data. Phys. Rev. A34, 2427–2432.

Theiler, J., 1990. Estimating fractal dimension. J. Opt. Soc. Am. A7, 1055–1073.

Thomson, B.D., Young, R.P., Lockner, A., 2009. Premonitory acoustic emissions and stick-slip in natural and smooth-faulted Westerly granite. J. Geophys. Res. 114, B02205.

Tselentis, G.A., Makroupoulos, K., Voulgaris, N., 1989. Cluster and spectral characteristics of the aftershock activity of the Kalamata, September 13, 1986 earthquake, South Greece. Tectonophysics 169, 135–148. https://doi.org/10.1016/0040-1951(89)90187-X.

Venturini, C., 1991. Cinematica neogenico-quaternaria del Sudalpino orientale (settore friulano). Studi Geol Camerti, Camerino 109–116. Vol. Spec.

Wiemer, S., 2001. A software package to analyze seismicity: ZMAP. Seismol. Res. Lett. 72, 374–383 (17, 36, 37 W).

Zaliapin, I., Ben-Zion, Y., 2013. Earthquake clusters in southern California I: Identification and stability. J. Geophys. Res. 118 (6), 2847–2864.

Zaliapin, I., Gabrielov, A., Wong, H., Keilis-Bork, V.I., 2008. Clustering analysis of seismicity and aftershock identification. Phys. Rev. Lett. 101, 018501.